ISSN 1392–1207. MECHANIKA. 2023 Volume 29(1): 12–18

Multiscale Analysis and Numerical Simulation of Hydrodynamic Inclined Fixed Pad Thrust Slider Bearing with Ultra Low Surface Separation Involving Surface Roughness

Weiwei ZHU, Chen HUANG, Chao WANG, Yongbin ZHANG
College of Mechanical Engineering, Changzhou University, Changzhou, Jiangsu Province, China,
E-mails: yongbinzhang@cczu.edu.cn; engmech1@sina.com (Corresponding author)

crossref http://dx.doi.org/10.5755/j02.mech.30821

1. Introduction

The development of modern industry has put forward higher requirements for the lubrication performance of hydrodynamic slider bearings. In fact, the manufactured bearing surface often has somewhat surface roughness. When the bearing surface roughness is comparable to the bearing clearance, the surface roughness should influence the bearing performance [1-3].

There have been a lot of studies on mixed lubrication by considering the surface roughness effect. It was ever popularly followed that in a hydrodynamic lubricated contact the load is carried by both the hydrodynamic film and the solid asperity contact [4-6]. There have been the arguments that such a model may be over simplified because of neglecting the effect of the physically adsorbed layer on the lubricated surface.

Molecular dynamics simulations (MDS) as well as experiments showed the existence of the physically adsorbed boundary layer in a hydrodynamic contact [7-10]. However, there were the difficulties in simulating the behavior of the adsorbed layer in an engineering hydrodynamic problem because of MDS taking over large cost of computer storage and computational time. In recent years, Zhang developed the closed-form explicit flow equations respectively for the adsorbed layer flow and the intermediate continuum fluid flow in the two-dimensional multiscale flow problem [11]. The advantage of this multiscale approach is to give fast solution and be able to solve the engineering problem.

The present paper attempts to study the effect of the surface roughness in the hydrodynamic inclined fixed pad thrust slider bearing with ultra low surface separations considering the physically adsorbed boundary layer. It is aimed to give the new results of the surface roughness influence on this mode of bearing.

2. Studied bearing

Fig. 1 shows the hydrodynamic inclined fixed pad thrust slider bearing with ultra low surface separation involving surface roughness. This bearing occurs when the load is very heavy and the bearing surface is not smooth so that there is only a very small gap between the bearing surfaces.

The upper surface of the bearing is stationary with the sinusoidal roughness, and the lower surface is assumed as perfectly smooth and moves with the speed u. The whole width of the bearing is l, and the tilting angle of the bearing is θ. The upper and lower surfaces are assumed as identical, and the adsorbed layers on both of them have the same thickness h_{bf}. The intermediate continuum fluid film thickness is h, the surface separation is h_{tot}, and that on the exit of the bearing is $h_{tot,o}$. The used coordinates are also shown in Fig. 1.

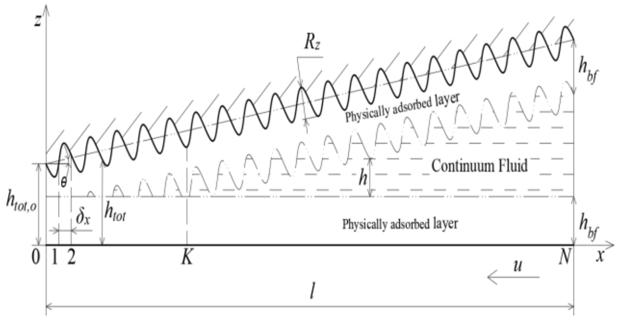

Fig. 1 Hydrodynamic inclined fixed pad thrust slider bearing with ultra low clearance involving surface roughness

3. Numerical analysis

Considering that the viscosity and density of the fluid will be affected by the pressure in this severe condition, the piezo-viscous effect of the fluid is considered in the present study. In addition to this, this study is based on the following assumptions: a) the side leakage is negligible; b) no interface slippage occurs on any interface; c) the flow is isothermal; d) the working condition is steady-state.

3.1. For the present bearing

According to the nanoscale flow equation [12], the total mass flow rate per unit contact length through the boundary lubrication area (without the intermediate continuum fluid film) is:

$$q_m = \frac{dp}{dx}\frac{S\rho_{bf,2}^{eff}h_{tot}^3}{12\eta_{bf,2}^{eff}} - \frac{u}{2}h_{tot}\rho_{bf,2}^{eff}, \tag{1}$$

where: $h_{tot} = h_{tot,o} + x\tan\theta + R_z\sin(\omega x+\varphi)/2$; p is the film pressure; $\rho_{bf,2}^{eff}$ and $\eta_{bf,2}^{eff}$ are respectively the average density and the effective viscosity of the adsorbed layer in the boundary lubrication area; S is the parameter accounting for the non-continuum effect of the adsorbed layer.

According to the multiscale flow equation [11], the total mass flow rate per unit contact length through the sandwich film lubrication area (with the intermediate continuum fluid film) is:

$$q_m = \frac{\rho_{bf,1}^{eff} h_{bf}^3}{\eta_{bf,1}^{eff}} \frac{dp}{dx} \left[\frac{F_1}{6} - \left(1 + \frac{1}{2\lambda_{bf}} - \frac{q_0 - q_0^n}{q_0^{n-1} - q_0^n} \frac{\Delta_{n-2}}{h_{bf}} \right) \frac{\varepsilon}{1 + \frac{\Delta x}{D}} \right] + \frac{\rho h^3}{\eta_{bf,1}^{eff}} \frac{dp}{dx} \left[\frac{F_2 \lambda_{bf}^2}{6} - \frac{\lambda_{bf}}{1 + \frac{\Delta x}{D}} \left(\frac{1}{2} + \lambda_{bf} - \frac{q_0 - q_0^n}{q_0^{n-1} - q_0^n} \frac{\Delta_{n-2} \lambda_{bf}}{h_{bf}} \right) \right] -$$

$$- u h_{bf} \rho_{bf,1}^{eff} - \frac{\rho h^3}{12\eta} \frac{dp}{dx} - \frac{\rho u h}{2}, \tag{2}$$

where: $\lambda_{bf} = h_{bf}/h$, n is the equivalent number of the fluid molecules across the adsorbed layer thickness; D and Δx are respectively the fluid molecule diameter and the separation between the neighboring fluid molecules in the adsorbed layer in the x coordinate direction; Δ_{n-2} is the separation between the neighboring fluid molecules across the adsorbed layer thickness just on the boundary between the adsorbed layer and the intermediate continuum fluid; ρ and η are respectively the bulk density and the bulk viscosity of the fluid; pressure; $\rho_{bf,2}^{eff}$ and $\eta_{bf,2}^{eff}$ are respectively the average density and the effective viscosity of the adsorbed layer in the sandwich film flow; $q_0 = \Delta_{j+1} / \Delta_j$; q_0 is averagely constant; Δ_j is the separation between the $(j+1)^{th}$ and j^{th} fluid molecules across the adsorbed layer thickness;

$F_1 = \eta_{bf,1}^{eff} \left(12 D^2 \Psi + 6 D \Phi \right) / h_{bf}^3$,

$F_2 = 6 \eta_{bf,1}^{eff} D (n-1) \left(l\Delta_{l-1} / \eta_{line,l-1} \right)_{avr,n-1} / h_{bf}^2$,

$\varepsilon = (2DI + II) / \left[h_{bf} (n-1) \left(\Delta_l / \eta_{line,l} \right)_{avr,n-1} \right]$, here

$I = \sum_{i=1}^{n-1} i \left(\Delta_l / \eta_{line,l} \right)_{avr,i}$, $\Psi = \sum_{i=1}^{n-1} i \left(l\Delta_{l-1} / \eta_{line,l-1} \right)_{avr,i}$,

$II = \sum_{i=0}^{n-2} \left[i(\Delta_l / \eta_{line,l})_{avr,i} + (i+1)(\Delta_l / \eta_{line,l})_{avr,i+1} \right] \Delta_i$,

$\Phi = \sum_{i=0}^{n-2} \left[i \left(l\Delta_{l-1} / \eta_{line,l-1} \right)_{avr,i} + (i+1) \left(l\Delta_{l-1} / \eta_{line,l-1} \right)_{avr,i+1} \right] \Delta_i$,

$i \left(\Delta_l / \eta_{line,l-1} \right)_{avr,i} = \sum_{j=1}^{i} \Delta_{j-1} / \eta_{line,j-1}$,

$i \left(l\Delta_{l-1} / \eta_{line,l-1} \right)_{avr,i} = \sum_{j=1}^{i} j\Delta_{j-1} / \eta_{line,j-1}$; $\eta_{line,j-1}$ is the local viscosity between the j^{th} and $(j-1)^{th}$ and fluid molecules across the adsorbed layer thickness, and $\eta_{line,j} / \eta_{line,j+1} = q_0^{\gamma}$.

The fluid bulk viscosity is expressed as: $\eta = \eta_a exp\left\{ (ln\eta_a + 9.67) \left[\left(1 + 5.1 \times 10^{-9} p \right)^G - 1 \right] \right\}$, where $G = \alpha / \left[5.1 \times 10^{-9} (ln\eta_a + 9.67) \right]$ and η_a is the fluid bulk viscosity at atmospheric pressure. The fluid bulk density is expressed as: $\rho = \rho_a (1 + \beta \cdot p)$, where ρ_a is the fluid bulk density at atmospheric pressure and β is constant.

As shown in Fig. 1, there are the $(N+1)$ discretized points evenly distributed in the whole area. According to Eq. (1), the pressure gradient on the K_{th} discretized point is:

$$\frac{dp}{dx}\Big|_K = \frac{p_K - p_{K-1}}{\delta_x} = \frac{12 \eta_{bf,2}^{eff} \left(q_m + \frac{u}{2} h_{tot,K} \rho_{bf,2}^{eff} \right)}{S \rho_{bf,2}^{eff} h_{tot,K}^3},$$

for $h_{tot,K} \le 2h_{bf}$. (3)

According to Eq. (2), the pressure gradient on the K^{th} discretized point is:

$$\frac{dp}{dx}\Big|_K = \frac{p_K - p_{K-1}}{\delta_x} = \frac{a\left(h_{tot,K} - 2h_{bf} \right) + b}{\left[c\left(h_{tot,K} - 2h_{bf} \right)^3 + d \right] cot\theta},$$

for $h_{tot,K} \le 2h_{bf}$. (4)

where: $h_{tot,K} = h_{tot,o} + x_K tan\theta + R_z sin(\omega x_K + \varphi)/2$; $a = up/2$, $b = q_m + u h_{bf} \rho_{bf,1}^{eff}$,

$$c = \frac{F_2 \lambda_{bf}^2 \rho tan\theta}{6 \eta_{bf,1}^{eff}} - \frac{\rho tan\theta}{12\eta} - \frac{\lambda_{bf} \rho tan\theta}{\eta_{bf,1}^{eff} \left(1 + \frac{\Delta x}{D} \right)} \left(\frac{1}{2} + \lambda_{bf} - \frac{q_0 - q_0^n}{q_0^{n-1} - q_0^n} \frac{\Delta_{n-2} \lambda_{bf}}{h_{bf}} \right), \tag{5}$$

$$d = \frac{h_{bf}^3 \rho_{bf,1}^{eff} F_1 tan\theta}{6 \eta_{bf,1}^{eff}} - \frac{h_{bf}^3 \rho_{bf,1}^{eff} tan\theta}{\eta_{bf,1}^{eff}} \left(1 + \frac{1}{2\lambda_{bf}} - \frac{q_0 - q_0^n}{q_0^{n-1} - q_0^n} \frac{\Delta_{n-2}}{h_{bf}} \right) \frac{\varepsilon}{1 + \frac{\Delta x}{D}}. \tag{6}$$

The backward difference gives that:

$$p_K - p_{K-1} = \frac{dp}{dx}\Big|_K \cdot \delta_x, \tag{7}$$

where: p_K and p_{K-1} are respectively the hydrodynamic pressures on the K^{th} and $(K\text{-}1)^{th}$ discretized points and $\delta_x = l/N$.

Since $p_0 = 0$, it is easily written that $p_K = \sum_{M=1}^{K} (p_M - p_{M-1})$, where:

$$p_M - p_{M-1} = \frac{12 \eta_{bf,2}^{eff} \left(q_m + \frac{u}{2} h_{tot,M} \rho_{bf,2}^{eff} \right)}{S \rho_{bf,2}^{eff} h_{tot,M}^3} \delta_x,$$

for $h_{tot,M} \le 2h_{bf}$, (8)

$$p_M - p_{M-1} = \frac{a\left(h_{tot,M} - 2h_{bf}\right) + b}{\left[c\left(h_{tot,M} - 2h_{bf}\right)^3 + d\right]\cot\theta}\delta_x,$$

for $h_{tot,M} > 2h_{bf}$. (9)

The load per unit contact length carried by the bearing is then calculated as:

$$w = \delta_x \sum_{K=1}^{N} p_K. \tag{10}$$

3.2. For the classical mode of the bearing

For comparison, the numerical analysis of the classical mode of the bearing (ignoring the adsorbed layer) is carried out in this section.

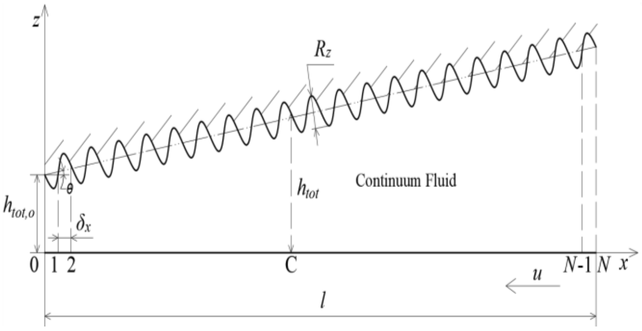

Fig. 2 The classical mode of the bearing with surface roughness

As shown in Fig. 2, for the classical mode of the bearing, there are the (N+1) discretized points evenly distributed in the whole area. The pressure gradient on the C^{th} discretized point is:

$$\frac{dp}{dx}\Big|_C = -\frac{6u\eta}{h_{tot,C}^2} - \frac{12\eta q_{m,C}}{\rho h_{tot,C}^3}, \tag{11}$$

where: $h_{tot,C}=h_{tot,o}+ x_C tan\theta + R_z sin(\omega x_C+\varphi)/2$ and $q_{m,C}$ is the mass flow rate per unit contact length in the classical mode of bearing.

The finite difference gives that $dp/dx\big|_C = (p_C - p_{C-1})/\delta_x$, p_C and $p_{C\text{-}1}$ are respectively the hydrodynamic pressures on the C^{th} and $(C–1)^{th}$ discretized points. Since p_0=0, it is easily written that $p_C = \sum_{j=1}^{C}\left(p_j - p_{j-1}\right)$. The pressure on the C^{th} discretized point is then:

$$p_C = -6\delta_x \sum_{j=1}^{C}\left(\frac{u\eta}{h_{tot,j}^2} + \frac{2\eta q_{m,C}}{\rho h_{tot,j}^3}\right),$$

for C = 1, 2,…, N. (12)

The load per unit contact length carried by the bearing is calculated as:

$$w = \delta_x \sum_{C=1}^{N} p_C. \tag{13}$$

3.3. Normalization

The dimensionless parameters are defined as follows: $\bar{\delta}_x = \frac{\delta_x}{h_{bf}}$, $\bar{\delta}_{x,C} = \frac{\delta_x}{h_{tot,o}}$, $H_{tot,M} = \frac{h_{tot,M}}{h_{bf}}$,

$$H_1 = \frac{h_{bf}}{h_{cr,bf,1}},\ H_2 = \frac{h_{tot}}{h_{cr,bf,2}},\ M_1 = \frac{\eta}{\eta_a},\ N_1 = \frac{\rho}{\rho_a},\ \bar{c} = \frac{c\eta_a}{\rho_a},$$

$$\bar{d} = \frac{d\eta_a}{\rho_a h_{bf}^3},\ Cy_1 = \frac{\eta_{bf,1}^{eff}}{\eta},\ Cy_2 = \frac{\eta_{bf,2}^{eff}}{\eta},\ Cq_1 = \frac{\rho_{bf,1}^{eff}}{\rho},$$

$$Cq_2 = \frac{\rho_{bf,2}^{eff}}{\rho},\ Q_m = \frac{q_m}{u\rho_a h_{tot,o}},\ P = \frac{ph_{tot,o}}{u\eta_a},\ W = \frac{w}{u\eta_a}.$$

Here $h_{cr,bf,1}$ is the critical thickness for characterizing the rheological properties of the adsorbed layer in the sandwich flow, and $h_{cr,bf,2}$ is the critical thickness for characterizing the rheological properties of the adsorbed layer in the boundary lubrication area.

3.3.1. For the present bearing

The dimensionless pressure on the K^{th} discretized point is: $P_K = \sum_{M=1}^{K}(P_M - P_{M-1})$, where:

$$P_M - P_{M-1} = \bar{\delta}_x\left(\frac{12Cy_2M_1Q_mH_{tot,o}^2}{SCq_2N_1H_{tot,M}^3} + \frac{6Cy_2M_1H_{tot,o}}{SH_{tot,M}^2}\right),$$

for $H_{tot,M} \le 2$, (14)

$$P_M - P_{M-1} = \\ = \bar{\delta}_x \frac{\left(H_{tot,M} - 2\right)H_{tot,o}N_1/2 + Cq_1H_{tot,o}N_1 + Q_mH_{tot,o}^2}{\left[\bar{c}\left(H_{tot,M} - 2\right)^3 + \bar{d}\right]cot\theta},$$

for $H_{tot,M} > 2$, (15)

where: Q_m is the dimensionless mass flow rate per unit contact length through the bearing:

$$\bar{c} = \frac{N_1F_2\lambda_{bf}^2 tan\theta}{6Cy_1M_1} - \frac{N_1 tan\theta}{12M_1} - \\ -\frac{\lambda_{bf}N_1 tan\theta}{Cy_1M_1\left(1+\frac{\Delta x}{D}\right)}\left(\frac{1}{2} + \lambda_{bf} - \frac{q_0 - q_0^n}{q_0^{n-1} - q_0^n}\frac{\Delta_{n-2}\lambda_{bf}}{h_{bf}}\right), \tag{16}$$

$$\bar{d} = \frac{Cq_1N_1F_1 tan\theta}{6Cy_1M_1} - \\ -\frac{Cq_1N_1 tan\theta}{Cy_1M_1}\left(1 + \frac{1}{2\lambda_{bf}} - \frac{q_0 - q_0^n}{q_0^{n-1} - q_0^n}\frac{\Delta_{n-2}}{h_{bf}}\right)\frac{\varepsilon}{1+\frac{\Delta x}{D}}, \tag{17}$$

The dimensionless load carried by the bearing is:

$$W = \bar{\delta}_x \sum_{K=1}^{N-1} P_K . \tag{18}$$

3.3.2. For the classical mode of bearing

The dimensionless pressure on the C^{th} discretized point is:

$$P_C = -6\bar{\delta}_{x,C} \sum_{j=1}^{C} \left(\frac{M_1}{H_{tot,j}^2} + \frac{2M_1 Q_{m,C}}{N_1 H_{tot,j}^3} \right),$$

$$\text{for } C = 1, 2, \ldots, N. \tag{19}$$

where: $Q_{m,c}$ is the dimensionless mass flow rate per unit contact length through this bearing.

The dimensionless load carried by the bearing is:

$$W = \bar{\delta}_{x,C} \sum_{C=1}^{N-1} P_C . \tag{20}$$

3.4. Numerical solution procedure

Fig. 2 shows the numerical solution procedure, from which it can be seen that the calculation results are converged by controlling the precision of Q_m. Then, substitute Q_m into Eqs. (14) or (15) to calculate the pressure on each discrete point, and get the final result for the present bearing. For the classical bearing, the numerical calculation method is the same.

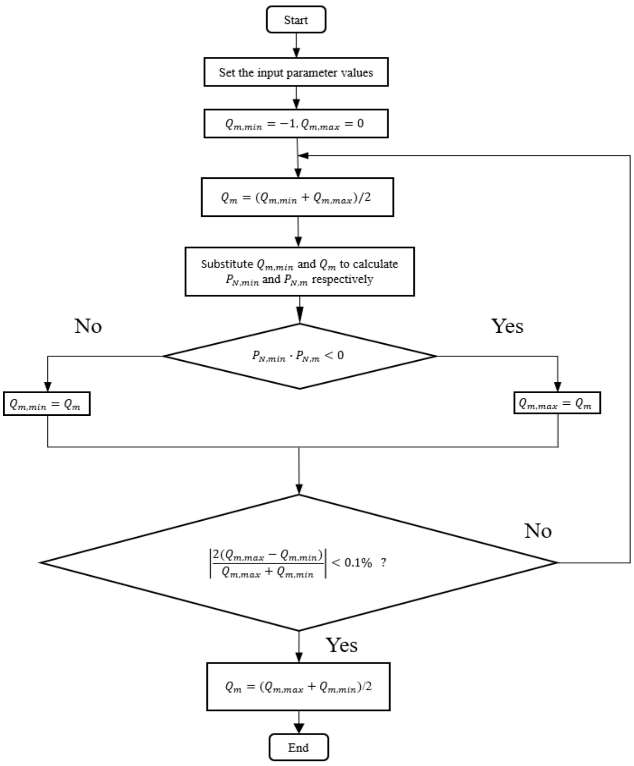

Fig. 3 The numerical solution procedure

4. Calculation

Exemplary calculations were carried out for the following input parameter values:

D = 0.5 nm; $\Delta_{n-2}/D = \Delta_x / D = 0.15$; l = 100 μm; $\theta = 1.0\times10^{-4}$ rad; $\alpha = 1.6\times10^{-8}$ m²/N; $\beta = 0.4\times10^{-9}$ Pa^{-1}; $u = 1\times10^{-6}$ m/s; $w = 2\pi/\lambda$; $\lambda = l/20$; $\varphi = \pi$; $\eta_a = 0.03$ Pa·s.

The parameters $Cq_1(H_1)$ and $Cq_2(H_2)$ are generally expressed by the following well used formula:

$$Cq(H) = \\ = \begin{cases} 1 & , \text{ for } H \geq 1 \\ m_0 + m_1 H + m_2 H^2 + m_3 H^3 & , \text{ for } 0 < H < 1 \end{cases}, \tag{21}$$

where: H is H_1 or H_2; m_0, m_1, m_2 and m_3 are respectively shown in Table 1.

The parameters $Cy_1(H_1)$ and $Cy_2(H_2)$ are generally expressed by the following well used formula:

$$Cy(H) = \begin{cases} 1 & , \text{ for } H \geq 1 \\ a_0 + \frac{a_1}{H} + \frac{a_2}{H^2} & , \text{ for } 0 < H < 1 \end{cases}, \tag{22}$$

where: H is H_1 or H_2; a_0, a_1 and a_2 are respectively shown in Table 2.

The parameter $S(H_2)$ is expressed by the following well used formula:

$$S(H_2) = \begin{cases} -1 & , \text{ for } H_2 \geq 1 \\ \left[n_0 + n_1 (H_2 - n_3)^{n_2} \right]^{-1} & , \text{ for } n_3 < H_2 < 1 \end{cases}, \tag{23}$$

where: n_0, n_1, n_2 and n_3 are respectively shown in Table 3.

The parameters F_1, F_2 and ε are respectively formulated as [11]:

$$F_1 = 0.18 \left(\frac{\Delta_{n-2}}{D} - 1.905 \right) \left(lnn - 7.897 \right), \tag{24}$$

$$F_2 = (-3.707E-4) \left(\frac{\Delta_{n-2}}{D} - 1.99 \right) (n + 64) \cdot \\ \cdot \left(q_0 + 0.19 \right) \left(\gamma + 42.43 \right), \tag{25}$$

$$\varepsilon = (4.56E-6) \left(\frac{\Delta_{n-2}}{D} + 31.419 \right) (n + 133.8) \cdot \\ \cdot (q_0 + 0.188)(\gamma + 41.62), \tag{26}$$

The weak, medium and strong fluid-bearing surface interactions were respectively used. They respectively have the operational parameter values shown in Tables 1-4.

Table 1

Popularly used fluid density data for different fluid-bearing surface interactions

Interaction \ Parameter	m_0	m_1	m_2	m_3
Strong	1.43	-1.723	2.641	-1.347
Medium	1.30	-1.065	1.336	-0.571
Weak	1.116	-0.328	0.253	-0.041

Table 2

Popularly used fluid viscosity data for different fluid-bearing surface interactions

Interaction \ Parameter	a_0	a_1	a_2
Strong	1.8335	-1.4252	0.5917
Medium	1.0822	-0.1758	0.0936
Weak	0.9507	0.0492	1.6447E-4

Table 3

Popularly used fluid non-continuum property data for different fluid-bearing surface interactions

Interaction \ Parameter	n_0	n_1	n_2	n_3
Strong	0.4	-1.374	-0.534	0.035
Medium	-0.649	-0.343	-0.665	0.035
Weak	-0.1	-0.892	-0.084	0.1

Table 4

Popularly used values of n, q_0, γ, $h_{cr,bf,1}$ and $h_{cr,bf,2}$ for different fluid-bearing surface interactions

Interaction \ Parameter	n	q_0	γ	$h_{cr,bf,1}$, nm	$h_{cr,bf,2}$, nm
Strong	8	1.2	1.5	40	80
Medium	5	1.1	1	20	40
Weak	3	1.03	0.5	7	14

5. Results

For the weak fluid-bearing surface interaction, in the bearing with $R_z > 13.4$ nm will occur the coexistence of the boundary lubrication and the sandwich film lubrication when $h_{tot,o}$ =10 nm. For $R_z < 13.4$ nm is only present the sandwich film lubrication. For medium and strong fluid-bearing surface interactions, the cases are similar respectively for $R_z > 8.96$ nm and $R_z > 2.72$ nm.

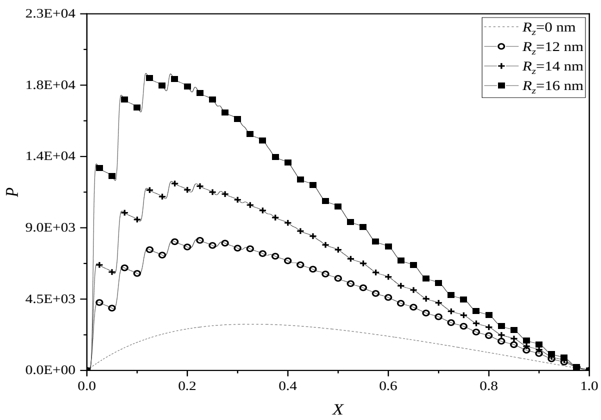

a) For the weak interaction

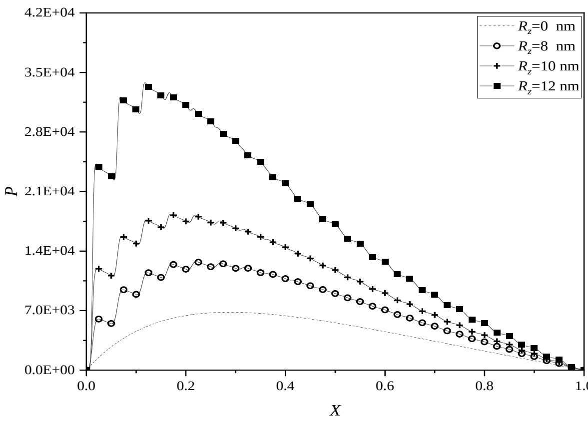

b) For the medium interaction

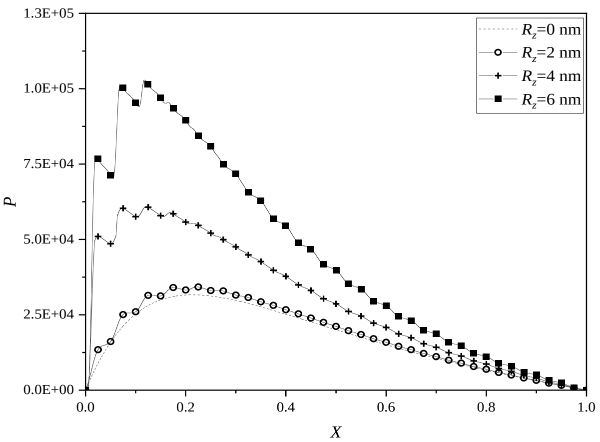

c) For the strong interaction

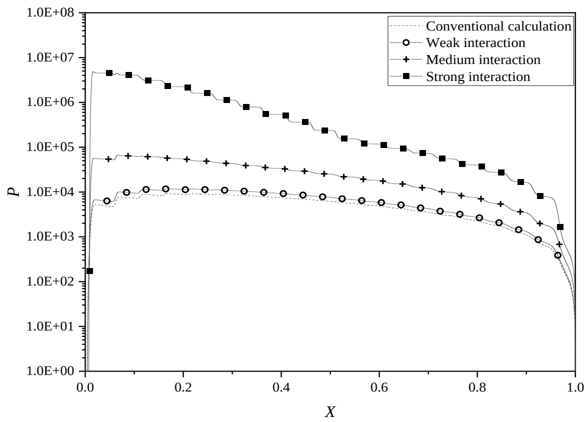

d) Pressure distributions for different fluid-bearing surface interactions (R_z = 14 nm)

Fig. 4 Dimensionless pressure distributions in the bearing for different surface roughness R_z and different fluid-bearing surface interactions when $h_{tot,o}$ =10 nm and $\theta = 1\times10^{-4}$ rad

5.1. Pressure distribution

Figs. 4, a-d plot the dimensionless pressure distributions in the bearing for different fluid-bearing surface interactions when the piezo-viscous effect is considered.

As shown in Figs. 4, a-c, the hydrodynamic pressure for the rough surface is always greater than that for the smooth surface, and the hydrodynamic pressure increases significantly with the increase of the surface roughness.

Fig. 4, d shows the pressure distributions in the bearing for different fluid-bearing surface interactions when $h_{tot,o}$ =10 nm and $R_z < 14$ nm. The results show that the hydrodynamic pressure for the weak interaction is less different from that calculated from classical hydrodynamic lubrication theory, while for the medium and strong interactions they are more different from the classical calculations. The pressure for the medium interaction is about 10 times larger than the classical calculation for the same operating condition, and the pressure for the strong interaction is about 1000 times larger than the classic calculation. It is shown that the adsorbed layer has a very significant effect on the pressure distribution in the bearing, stronger the fluid-bearing surface interaction, more obvious the effect of the adsorbed layer on the hydrodynamic pressure.

Fig. 5 shows the comparison between the pressure distributions with and without the piezo-viscous effect respectively for the strong interaction in the present bearing and for the classical calculation when R_z is 14nm. The pressure under the piezo-viscous effect is higher than that without the piezo-viscous effect for the strong interaction in the present bearing. The results show that the piezo-viscous effect cannot be ignored for the strong interaction in the present bearing.

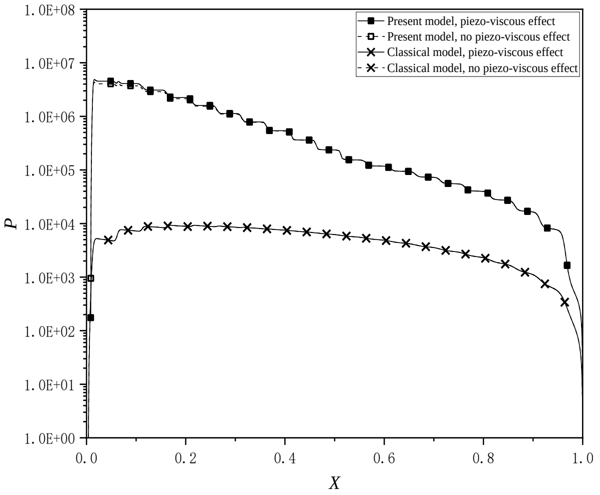

Fig. 5 Piezo-viscous effects in the present bearing for the strong interaction and in the classical bearing when $h_{tot,o}$ =10 nm and $\theta = 1\times10^{-4}$ rad

5.2. Carried load of the bearing

Fig. 6 shows the dimensionless carried loads of the bearing with the fluid piezo-viscous effect for different fluid-bearing surface interactions when $h_{tot,o}$ = =10 nm. With the increase of the surface roughness, the carried load of the bearing is increased significantly. It can be seen that the surface roughness very significantly improves the load-carrying capacity of the present bearing especially for the medium and strong interactions.

6. Conclusions

The multiscale calculation was numerically made for the pressure and carried load of the inclined fixed pad thrust slider bearing with ultra low surface separation involving the sinusoidal surface roughness on the stationary surface based on Zhang's multiscale approach and mixed lubrication model [11, 12]. In the present bearing, there are both the boundary lubrication and the sandwich film lubrication.

Based on the obtained results, the conclusions are drawn as follows:

a) The physically adsorbed layer has a very significant effect on the pressure distribution and the carried load of the bearing. The pressure distribution and carried load of the bearing are increased with the increase of the fluid-bearing surface interaction strength.

b) The bearing pressure and load capacity are increased significantly with the increase of the surface roughness. Especially for the strong fluid-bearing surface interaction, the fluid piezo-viscous effect significantly increases the bearing pressures and loads.

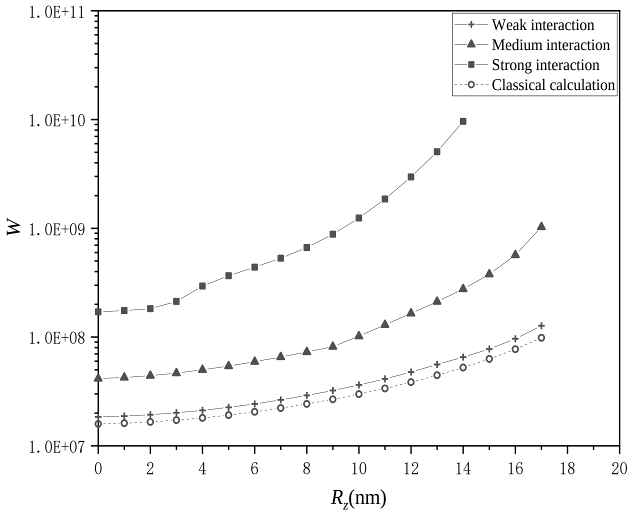

Fig. 6 Variation of the dimensionless carried load of the bearing with the surface roughness for different fluid-bearing surface interactions

References

1. **Li, C.; Wang, H. H.; Ren X. X.;** et al. 2014. Analysis of elastohydrodynamic lubrication of clamping ball screw of all-electric injection, Applied Mechanics and Materials 3468: 751-754. https://doi.org/10.4028/www.scientific.net/AMM.644-650.751.
2. **Xie, Z.; Rao, Z. S.; Ta, N.;** et al. 2016. Investigations on transitions of lubrication states for water lubricated bearing. Part II: further insight into the film thickness ratio lambda, Industrial Lubrication and Tribology 68(3): 416-429. https://doi.org/10.1108/ILT-10-2015-0147.
3. **Pang, X.; Jiang, W.; Jin ,X. W.** 2019. Investigation on lubrication state of sliding bearings in low-speed rotor system subjected to torque load, International Journal of Rotating Machinery 2019: 1-11. https://doi.org/10.1155/2019/1791830,
4. **Minet, C.; Brunetière, N.; Tournerie, B.** 2011. A deterministic mixed lubrication model for mechanical seals, Journal of Tribology-Transactions of the ASME 133(4): 042203. https://doi.org/10.1115/1.4005068.
5. **Holmes, M. J. A.; Evans, H. P.; Snidle, R. W.** 2005. Analysis of mixed lubrication effects in simulated gear tooth contacts, Journal of Tribology-Transactions of the ASME 127(1): 61–69. https://doi.org/10.1115/1.1828452.

6. **Patel, R.; Khan, Z. A.; Saeed, A.; Bakolas, V.** 2022. A review of mixed lubrication modelling and simulation, Tribology in Industry 44 (1): 150-168. https://doi.org/10.24874/ti.1186.09.21.11.
7. **Yen, T. H.; Soong, C. Y.; Tzeng, P. Y.** 2007. Hybrid molecular dynamics-continuum simulation for nano/mesoscale channel flows, Microfluidics and Nanofluidics 3(6): 665-675. https://doi.org/10.1007/s10404-007-0202-3.
8. **Liu, J.; Chen, S.; Nie, X.; Robbins, M. O.** 2007. A continuum-atomistic simulation of heat transfer in micro- and nano- flows, Journal of Computational Physics 227(1): 279-291. https://doi.org/10.1016/j.jcp.2007.07.014.
9. **Chauveteau, G.; Tirrell, M.; Omari, A.** 1984. Concentration dependence of the effective viscosity of polymer solutions in small pores with repulsive or attractive walls, Journal of Colloid and Interface Science 100: 41-54. https://doi.org/10.1016/0021-9797(84)90410-7.
10. **Cheng, S.; Luan, B.; Robbins, M. O.** 2010. Contact and friction of nanoasperities: Effects of adsorbed monolayers, Physical Review E 81: 016102. https://doi.org/10.1103/PhysRevE.81.016102.
11. **Zhang, Y. B.** 2020. Modeling of flow in a very small surface separation, Applied Mathematical Modeling 82: 573-586. https://doi.org/10.1016/j.apm.2020.01.069.
12. **Zhang, Y. B.** 2016. The flow equation for a nanoscale fluid flow, International Journal of Heat and Mass Transfer 92: 1004-1008. https://doi.org/10.1016/j.ijheatmasstransfer.2015.09.008.

W. Zhu, C. Huang, C. Wang, Y. Zhang

MULTISCALE ANALYSIS AND NUMERICAL SIMULATION OF HYDRODYNAMIC INCLINED FIXED PAD THRUST SLIDER BEARING WITH ULTRA LOW SURFACE SEPARATION INVOLVING SURFACE ROUGHNESS

S u m m a r y

In this paper, the hydrodynamic effect in the tilting fixed pad thrust slider bearing with ultra low surface separations is studied by the multiscale analysis considering the nanoscale surface roughness. The flow in the bearing is essentially multiscale incorporating both the adsorbed boundary layer flow and the intermediate continuum fluid flow. The numerical calculation results show that even the surface roughness on the 1nm scale has a strong influence on the generated pressure and carried load of the bearing, and the surface roughness effect strongly depends on the fluid-bearing surface interaction.

Keywords: adsorbed layer, hydrodynamic bearing, load, multiscale, surface roughness.

Received February 28, 2022
Accepted January 27, 2023